World Electric Vehicle Journal

MDPI

Article

Direct Instantaneous Torque Control of SRM Based on a Novel Multilevel Converter for Low Torque Ripple

Yan Cai [1,*], Zhongshan Dong [2,*], Hui Liu [2], Yunhu Liu [2] and Yuhang Wu [2]

[1] Tianjin Key Laboratory of Intelligent Control of Electrical Equipment, Tiangong University, Tianjin 300387, China
[2] School of Electrical Engineering, Tiangong University, Tianjin 300387, China; 2131070867@tiangong.edu.cn (H.L.); 2131070891@tiangong.edu.cn (Y.L.); wyhang1996@126.com (Y.W.)
* Correspondence: caiyan_tj@163.com (Y.C.); dongzhongshan492@163.com (Z.D.)

Abstract: The torque ripple of a switched reluctance motor (SRM) limits its application in electric vehicles. This paper proposes a DITC system for SRMs based on a novel multilevel converter (MLC), which aims at the problem that the torque ripple cannot be effectively suppressed for the conventional direct instantaneous torque control (DITC) of an SRM due to the limitation of the DC bus voltage in the asymmetric half-bridge converter (AHBC) and the single control strategy formulated in the commutation region. Based on the advantages of fast excitation and fast demagnetization for the proposed MLC and the torque distribution characteristics for each phase winding in the commutation region, a novel torque hysteresis control strategy is developed to improve the torque-following ability of the DITC and achieve the purpose of minimizing the torque ripple in the commutation region. In addition, multiobjective optimization control of the motor is carried out to improve the efficiency of the DITC system while suppressing the torque ripple. The effectiveness of the proposed SRM drive scheme is verified by experiment, which is of great significance for the application of SRMs in electric vehicles.

Keywords: switched reluctance motor; direct instantaneous torque control; multilevel converter; torque ripple; multiobjective optimization

Citation: Cai, Y.; Dong, Z.; Liu, H.; Liu, Y.; Wu, Y. Direct Instantaneous Torque Control of SRM Based on a Novel Multilevel Converter for Low Torque Ripple. *World Electr. Veh. J.* **2023**, *14*, 140. https://doi.org/10.3390/wevj14060140

Academic Editors: Xinmin Li and Liyan Guo

Received: 27 April 2023
Revised: 24 May 2023
Accepted: 25 May 2023
Published: 27 May 2023

1. Introduction

A switched reluctance motor (SRM) is very suitable for traction motors of electric vehicles due to its simple and robust structure, high fault tolerance, high starting torque, and great speed regulation performance [1–4]. However, its double salient pole structure and magnetic saturation characteristics cause torque ripple, resulting in vibration and noise, which affects the operational stability and comfort of electric vehicles [5–7]. Therefore, torque ripple suppression in SRMs is a critical research problem for scholars.

Optimizing the structure [8–10] and control [11–16] of SRMs are two ways to reduce the ripple. Among them, advanced control strategies are more commonly used and effective. Although average torque control (ATC) [17,18] is simple and widely used in SRMs, it is difficult to apply on the occasions where low torque ripple is required. Compared with ATC, instantaneous torque control enables precise torque control and can significantly suppress the torque ripple. Depending on the control method, instantaneous torque control includes indirect instantaneous torque control (IITC) [19–21] and direct instantaneous torque control (DITC) [22–24]. IITC generally calculates phase reference torque with a torque-sharing function (TSF) [25], from which the exact reference current is obtained, and then controls phase torque indirectly by adjusting each phase current to follow the phase reference current through a current controller. Compared with IITC, the controlled object of DITC is the instantaneous torque, which generates the switching signal based on the error between the reference torque and the instantaneous torque without precisely controlling the phase current, thus simplifying the control system structure and reducing the algorithm

implementation difficulty. Based on the conventional DITC, many scholars have proposed some novel DITC methods by improving the controller or combining advanced control theories. In [26], a fractional order proportional-integral-derivative (PID) controller is used instead of a conventional PID controller, which reduces the overshoot and adjustment time. In [27–29], some DITC methods combined with PWM are used to adjust the voltage duty ratio of each phase based on the torque error to obtain a suitable voltage vector, which suppresses the current ripple at low speed, thereby minimizing the torque ripple. In [30], a DITC method with an adaptive dynamic commutation strategy is proposed to dynamically control the commutation process by modifying the switching angles, which can achieve a reasonable distribution of phase torque and thus minimize the torque ripple.

Although these DITC methods can improve torque ripple in an SRM, when the motor operates at high speed, the phase current increases and decreases slowly due to the limitation of the DC bus voltage in the AHBC, resulting in a decrease in the torque-following ability of the DITC, which not only increases the torque ripple in the system but also affects the dynamic response performance and drive efficiency. In [31,32], a four-level converter is used for the DITC system. This four-level converter has the capability of high-voltage excitation and high-voltage demagnetization, which can reduce the rise and fall time of the current and thus improve the dynamic performance and efficiency of the system. However, each phase bridge arm of the four-level converter cannot operate independently, which not only limits the formulation of control strategy but also affects the suppression effect of the torque ripple in the commutation region.

In this article, a novel MLC is proposed in which each phase bridge arm can operate independently, and a DITC system for SRMs is designed using this MLC. By developing a novel control strategy, the torque-following capability of the DITC is improved, and the torque ripple of SRM is significantly reduced in a wide speed range. In addition, multiobjective optimization control is carried out to improve the efficiency of the DITC system while suppressing the torque ripple. Simulation study and experiment comparison demonstrate the effectiveness of the novel DITC.

2. Conventional DITC for SRM

2.1. Asymmetrical Half-Bridge Converter

The conventional DITC system usually uses an AHBC to drive the SRM. Each phase winding can operate in the three-level states with excitation (+1), freewheeling (0), and demagnetization (−1) by controlling the on or off of two switching devices in each phase bridge arm of the AHBC. These are illustrated in Figure 1.

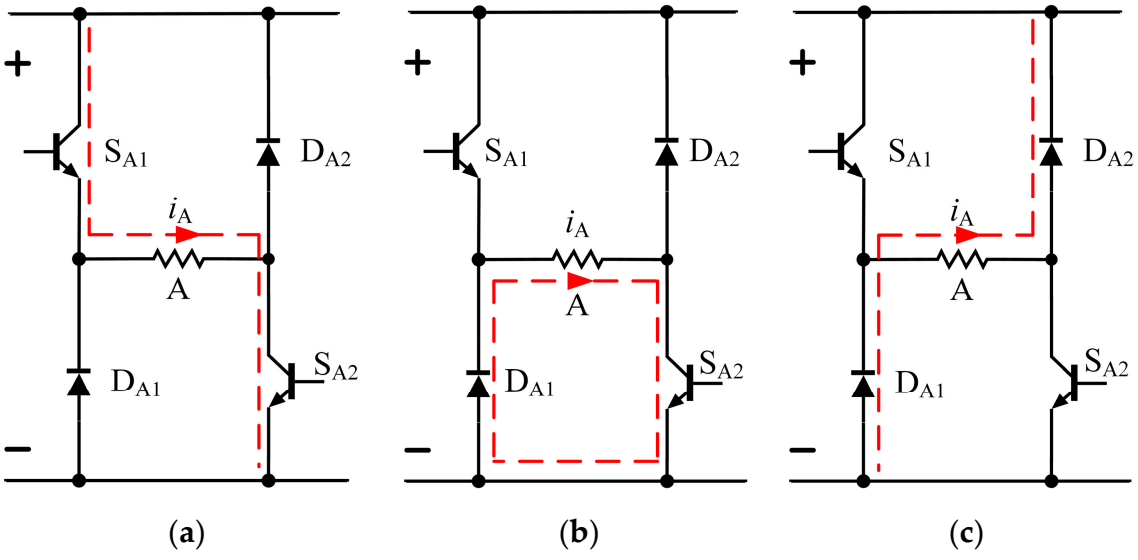

Figure 1. Operating states of the AHBC: (**a**) +1 state; (**b**) 0 state; (**c**) −1 state.

2.2. Conventional DITC System and Control Method for SRM

Figure 2 shows the inductance and current characteristic curves for each phase of the three-phase SRM. The DITC system turns on and turns off each phase winding according to rotor position, and three-phase windings are conducted once in rotation during an electrical cycle, where each one-third of an electrical period consists of a commutation region and a single-phase conduction region. As can be seen from the diagram, the commutation region is between the turn-on angle (θ_{on_b}) of phase B (following phase) and the maximum inductance (θ_a) of phase A (preceding phase), where the inductances of both phases A and B are rising, and two phases together produce positive torque required by the motor. The single-phase conduction region is between the θ_a and the turn-on angle (θ_{on_c}) of phase C. In this region, phase A enters the falling inductance region, and phase B remains in the rising inductance region, hence phase B alone provides positive torque.

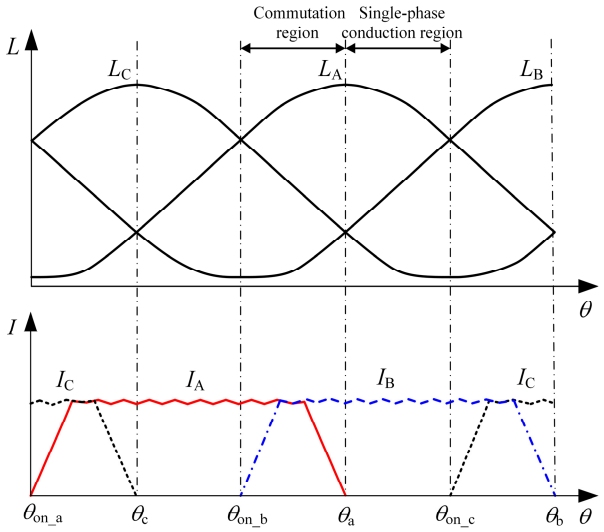

Figure 2. The inductance and current characteristic curves for each phase of the three-phase SRM.

The control structure of the conventional DITC system is presented in Figure 3, where the torque hysteresis controller is the key, which sets up the hysteresis control strategy for the commutation region and the single-phase conduction region. Figure 4 presents the control strategy. The vertical axis represents the operating state of each phase. The horizontal axis represents the error between the reference torque and the instantaneous torque, and the hysteresis thresholds ($-T_H$, $-T_L$, 0, T_L, and T_H) are defined based on its value The solid and dashed arrows represent the transfer direction of the torque error. During the operation of the DITC system, the torque hysteresis controller selects different operating states to adjust each phase torque based on rotor position, torque error, and transfer direction of torque error in order to make synthesized torque follow the reference torque.

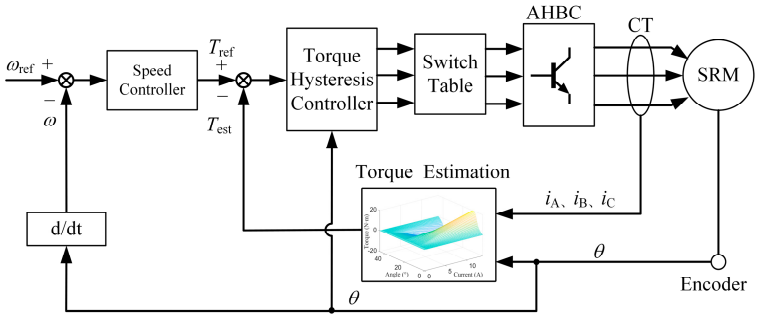

Figure 3. Control diagram for the conventional DITC system.

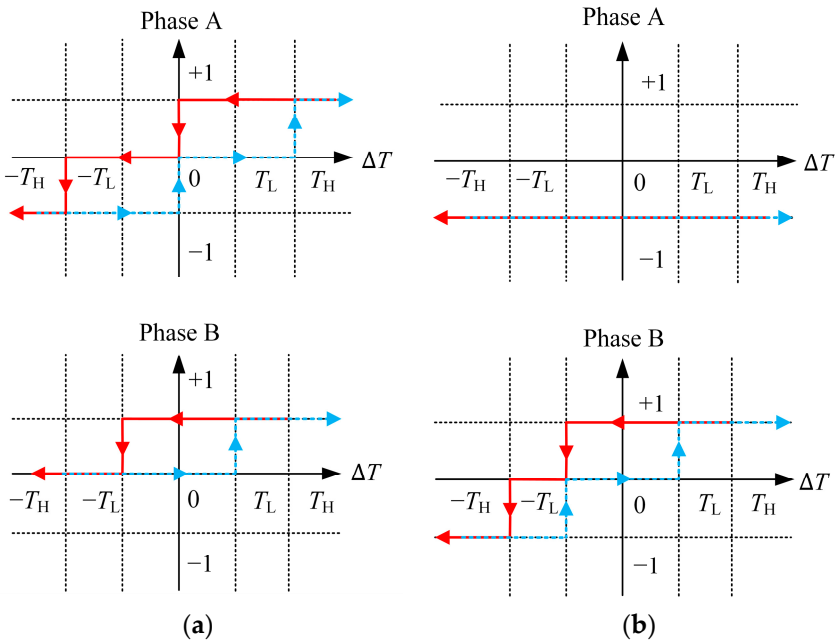

Figure 4. Conventional torque hysteresis control strategy: (**a**) control strategy in the commutation region; (**b**) control strategy in the single-phase conduction region.

When qualitatively analyzing the torque output characteristics of phase winding based on the inductance characteristics, the magnetic saturation is ignored and the phase inductance is considered to be related to the rotor position only; so the phase torque of SRM can be expressed by the following formula:

$$T_k(\theta, i_k) = \frac{1}{2} {i_k}^2 \frac{dL_k}{d\theta} \tag{1}$$

where T_k is phase torque, i_k is phase current, and L_k is phase inductance. Based on the torque expression, since the current and inductance of each phase winding in the commutation region constantly change, it is difficult to maintain a constant synthesized torque using a single control strategy.

The conventional DITC strategy makes the preceding phase work in the external hysteresis loop and the following phase work in the internal hysteresis loop without considering the torque output capacity per phase in the commutation region, and the torque error easily enters the external hysteresis loop. Thus, the torque ripple is noticeable in the commutation region. Additionally, SRMs operate at low speed where the phase current can be increased and decreased as expected, so the output torque is able to follow the reference torque. Nevertheless, as the speed increases, the rotating electric potential of winding increases, and the excitation and demagnetization time shorten, with the result that the current increases and decreases slowly so that the output torque has difficulty following the reference torque. The simulation waveforms are shown in Figure 5 for the conventional DITC system at 1250 r/min and 5 N·m load, with the torque error trajectory, phase torque, and phase voltage waveforms from top to bottom. At the beginning of commutation, the following phase is usually turned on near the minimum inductance to increase the current quickly. The change rate of inductance for the following phase is very low, and its current has yet to be fully built up. The torque generated by the following phase is not sufficient according to Formula (1), resulting in a significant torque error that exceeds T_H. At the end of commutation, the following phase experiences an increase in the change rate of inductance; at this point, the inductance of the preceding phase is still increasing, which leads to excess output torque due to its slow current decrease, causing the torque error to exceed $-T_H$ significantly. In addition, the current tailing of the preceding phase

enters the falling inductance region, resulting in the generation of negative torque; since the negative torque needs to be compensated by the positive torque in the single-phase conduction region, the efficiency of the motor is reduced.

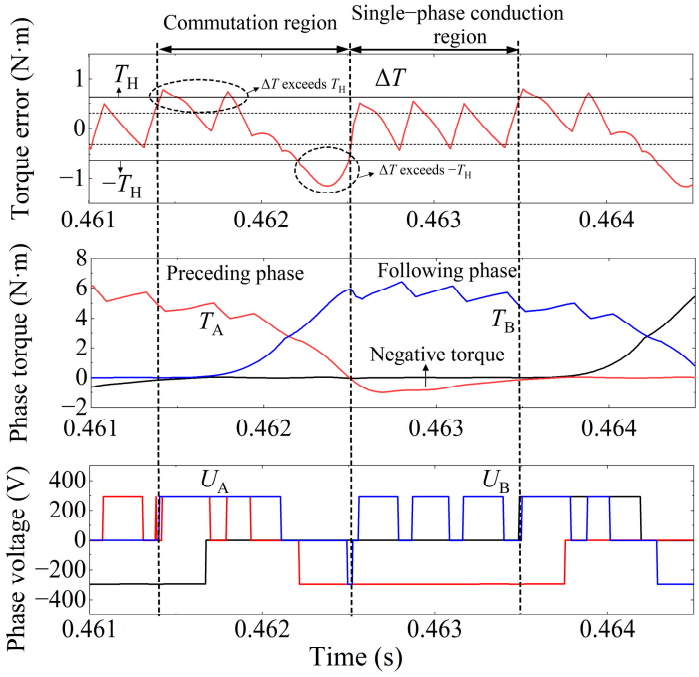

Figure 5. Simulation waveforms in the conventional DITC system at 1250 r/min and 5 N·m load.

In summary, to effectively minimize the torque ripple in an SRM, the optimization of control strategy is certainly important, but it is also necessary to improve the excitation and demagnetization speed of the converter on the motor windings so as to improve the torque-following capability of the DITC.

3. Novel Multilevel Converter

This paper proposes a novel MLC with a double bus structure, and the topology is shown in Figure 6. The MLC adds one switching device and one diode per phase of the bridge arm on the basis of the AHBC and adds a boost capacitor (C2) connected in series with the voltage-stabilizing capacitor (C1) at the DC power supply side. The bus connected to the positive terminal of C2 is called the high-voltage bus, and its voltage (U_{DC} + U_{C2}) equals the sum of the C2 voltage and DC voltage. The bus connected to the positive terminal of the power supply is called the DC bus.

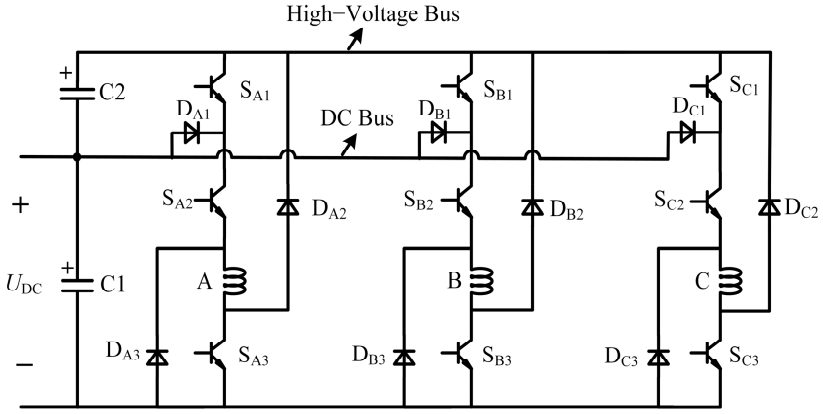

Figure 6. Topology of the novel multilevel converter.

Four operating states can be obtained with the on–off control of three switching devices in each bridge arm of the novel MLC, defined as the +2, +1, 0, and −2 states, as shown in Figure 7. For example, when all switching devices in the A-phase bridge arm are on, the winding operates in the +2 state, and the phase current can be ramped up more rapidly. The conduction path is shown in Figure 7a. When S_{A1} is off, S_{A2} and S_{A3} are on, and the winding operates in the +1 state; compared with the +2 state, the current is increased slowly, and the conduction path is shown in Figure 7b. When S_{A1} and S_{A2} are off, S_{A3} is on, the winding operates in the 0 state, and the conduction path is shown in Figure 7c. When all switching devices in the A-phase bridge arm are off, the winding operates in the −2 state, and the current can be decreased more quickly. The conduction path is shown in Figure 7d.

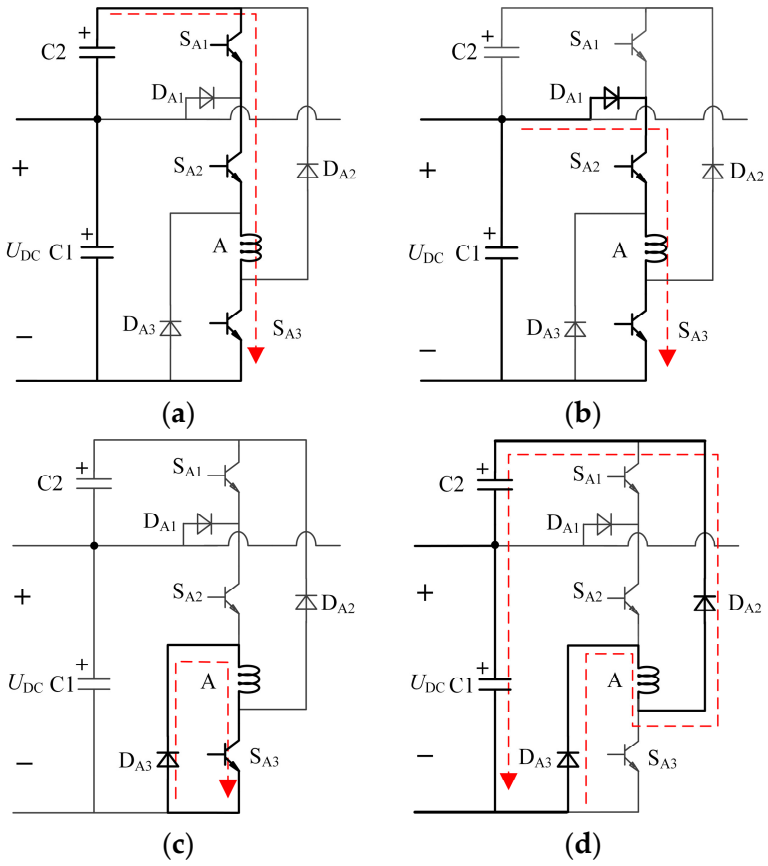

Figure 7. Operating states of the novel MLC: (**a**) +2 state; (**b**) +1 state; (**c**) 0 state; (**d**) −2 state.

The novel MLC enables multilevel driving for the SRM, and each bridge arm can operate independently, hence allowing flexible control strategies. In addition, during the winding demagnetization stage, C2 is used to recover the residual winding magnetic energy to achieve higher voltage. This structure does not require a front boost circuit, which can save costs.

4. DITC for SRMs with the Novel Multilevel Converter

Based on the novel MLC, a novel DITC system for SRMs is designed, as shown in Figure 8. The system mainly includes a torque hysteresis controller, torque calculation unit, boost voltage controller, novel MLC, and switch table. The torque hysteresis controller requires input parameters, including ΔT, θ, θ_{on}, θ_{off}, and θ_h. ΔT is the error in T_{ref} and T_{est}; T_{ref} is gained from the speed controller, and T_{est} is determined by using a lookup table in the torque calculation unit. θ is the rotor position, θ_{on} is the turn-on angle, and θ_{off} is the turn-off angle. θ_h is defined as the control angle that maintains the voltage stability of the high-voltage bus, and $[\theta_{on}, \theta_h]$ is defined as the region where +2 is used. For the three-phase 12/8 SRM, θ_h is located between $[\theta_{on}, \theta_{on} + 15°]$ and is determined by the boost

voltage controller according to U_{C2}, V_{ref}, θ_{on}, and θ. U_{C2} is the instantaneous voltage of C2, and V_{ref} is the reference voltage of C2. During the operation of the novel DITC system, the torque hysteresis controller determines the operating state for each phase winding based on θ_{on}, θ_{off}, θ_h, ΔT, and θ. Then, the switch table generates the drive signal for the converter, and the converter operates to realize the DITC for the SRM.

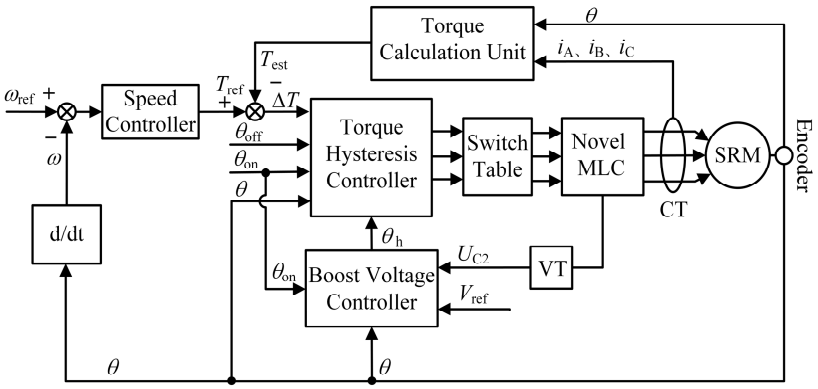

Figure 8. Control structure of the novel DITC system.

4.1. Torque Hysteresis Control Strategy with the Novel Multilevel Converter

To solve the problem that the motor output performance suffers due to the single control strategy for the conventional DITC in the commutation region and the DC bus voltage limitation of the AHBC, a novel control strategy is developed with the torque distribution characteristics of each phase in the commutation region and the advantages of fast excitation and fast demagnetization for the novel MLC. Shown at the same current value, Figure 9 illustrates the torque distribution of phases A and B in the commutation region for a three-phase 12/8 SRM. It is noticeable that the torque output capacity of phase A is strong in the early stage of commutation, and its current per ampere can generate greater output torque than that of phase B. In addition, phase B is currently in the current build-up stage, and its current is smaller. Therefore, in the early stage of commutation, phase A mainly provides the total electromagnetic torque. As the rotor position increases, the torque output capacity of phase A gradually decreases, and that of phase B gradually increases, and can produce larger output torque per ampere of current than that of phase A. Additionally, the current in phase B is fully established, while the current in phase A should be decreased to zero in time as phase A approaches its maximum inductance position. Therefore, phase B mainly provides the total electromagnetic torque in the late stage of commutation.

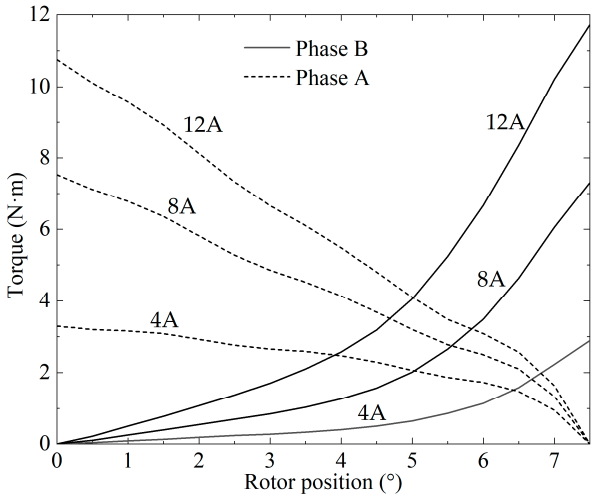

Figure 9. Torque distribution of phases A and B for a three-phase 12/8 SRM.

Hence, the commutation region is divided into Region I and Region II, according to the torque output capability of the preceding and following phases. Furthermore, the single-phase conduction region is now Region III. Each region is illustrated in Figure 10.

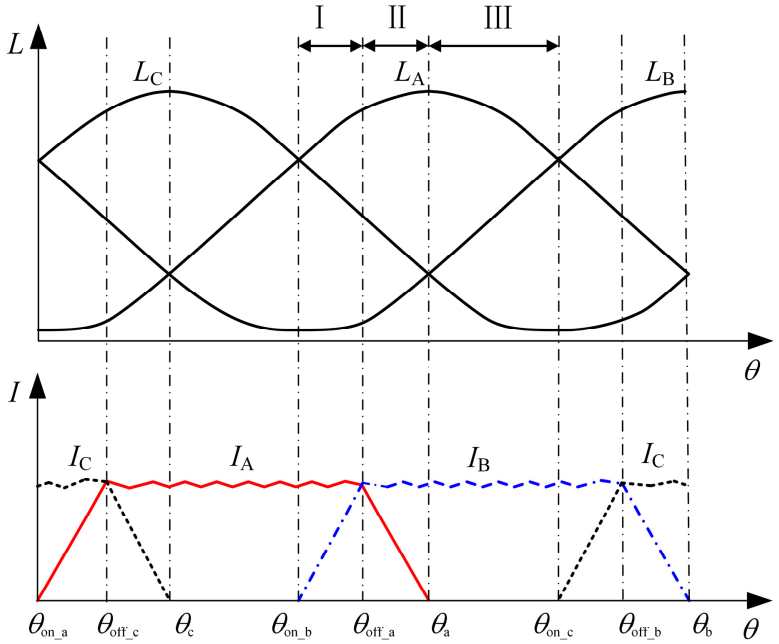

Figure 10. Regional division method for the novel DITC strategy.

Taking the commutation between phases A and B and the single-phase conduction of phase B as an example, the novel torque hysteresis control strategy for each region is presented in Figure 11. The excitation state of phase B in each region is represented by +n, which represents either the +2 state or the +1 state, and the state logic of +n depends on the location of θ_h. θ_h is between [θ_{on_b}, θ_{on_c}], +n is +2 within [θ_{on_b}, θ_h], and +n is +1 within [θ_h, θ_{on_c}], as shown in Figure 12 from the implementation waveform of the novel control strategy.

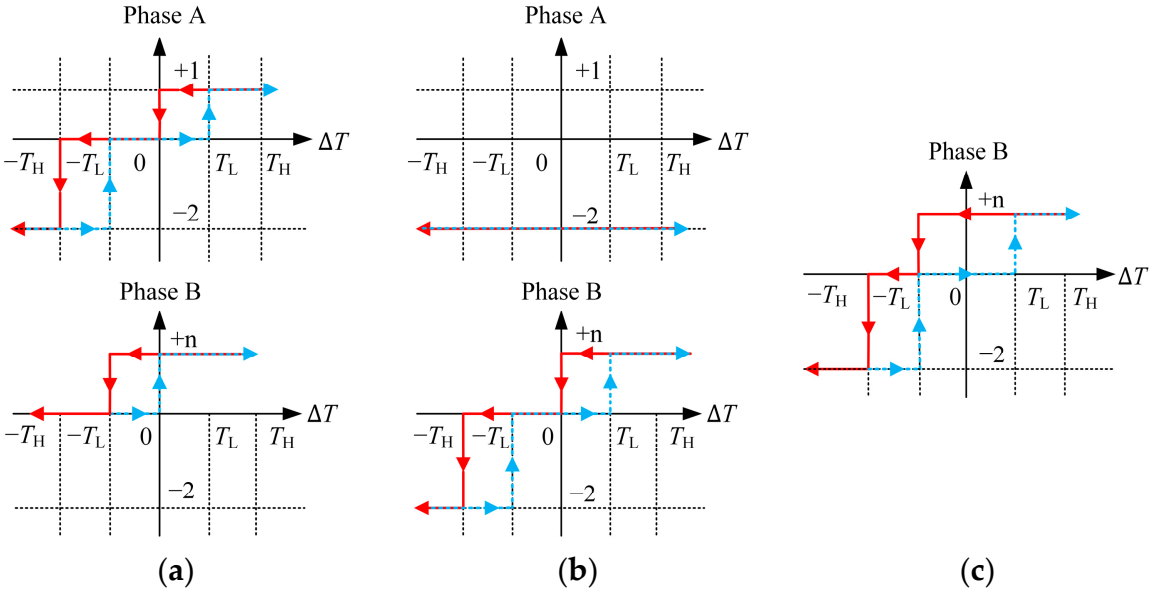

Figure 11. Novel torque hysteresis control strategy in each region: (**a**) Region I; (**b**) Region II; (**c**) Region III.

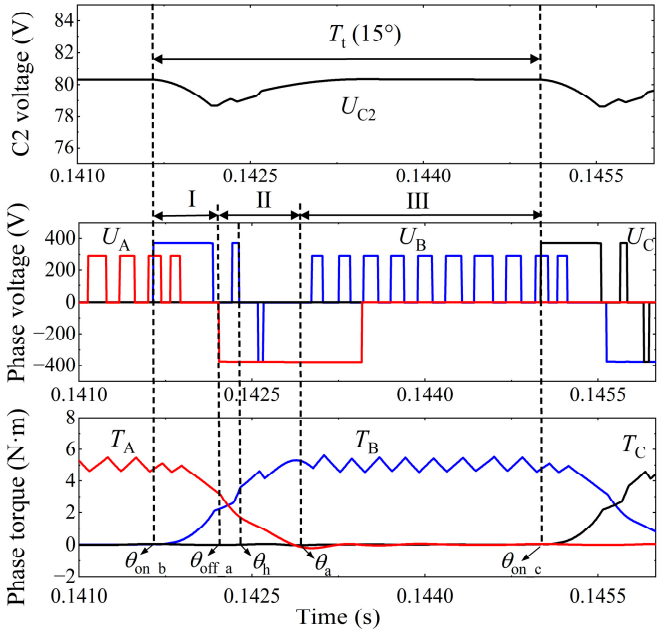

Figure 12. Implementation waveforms with the novel torque hysteresis control strategy in one-third of the electrical cycle.

The control strategy for Region I is shown in Figure 11a. When the total electromagnetic torque needs to be increased or decreased, the strategy is executed in priority between the internal hysteresis loop of phase A ($0 \leftrightarrow T_L$). Since phase A has a higher torque output capacity per ampere of current and the total electromagnetic torque is primarily available from phase A, this is conducive to improving the torque response speed and electromechanical conversion efficiency of the system. Phase B increases current preferentially in the +2 state, which allows the current in the following phase of the commutation region to build up more quickly than with the AHBC. When the output torque needs to be further reduced, i.e., ΔT decreases to $-T_L$ along the negative horizontal axis, phase B enters the 0 state and reduces the output torque together with phase A. If ΔT continues to decrease along the horizontal axis to $-T_H$, phase A enters the -2 state and rapidly reduces the output torque. While ΔT returns to zero along the positive horizontal axis, phase B returns to the excitation state.

The control strategy for Region II is shown in Figure 11b. When the total electromagnetic torque needs to be increased or decreased, the strategy is executed in priority between the internal hysteresis loop of phase B ($0 \leftrightarrow T_L$). Since phase B has a higher torque output capacity per ampere of current and the total electromagnetic torque is primarily available from phase B, this is conducive to improving the torque response speed and electromechanical conversion efficiency of the system. When ΔT decreases to $-T_H$ along the negative horizontal axis, phase B is in the -2 state to rapidly reduce the output torque. Phase A enters the -2 state in Region II to reduce the current tailing and avoid generating negative torque, which allows the current in the preceding phase of the commutation region to decrease to zero more quickly than with the AHBC.

The control strategy for Region III is shown in Figure 11c. When the total electromagnetic torque needs to be increased or decreased, the strategy is executed in priority between the internal hysteresis loop of phase B ($-T_L \leftrightarrow T_L$). If ΔT decreases to $-T_H$ along the negative horizontal axis, phase B is in the -2 state to rapidly reduce the output torque.

4.2. Stability Control of the High-Voltage Bus Voltage

The novel DITC system enhances the torque-following capability by fast excitation and fast demagnetization of phase windings, but this involves charging and discharging of C2, which leads to fluctuations in the high-voltage bus voltage. Therefore, to guarantee the

stability of the control system, stable control of the high-voltage bus voltage is necessary. According to Figure 6, the high-voltage bus voltage equals the sum of U_{C2} and U_{DC}. Under the condition that U_{DC} remains stable and its ripple is small, the stability of the high-voltage bus voltage mainly depends on the stability of U_{C2}. In this article, the stable control of the high-voltage bus voltage is realized by the boost voltage controller, and its structure is presented in Figure 13. The U_{C2} is collected by the voltage transducer (VT) and is calculated by the average voltage calculation unit based on θ_{on} and θ to obtain V_{av}; as shown in Figure 12, V_{av} is the average voltage of C2 in T_t. Additionally, the controller adjusts the error between V_{av} and V_{ref} by PI, limits the amplitude, and outputs θ_h. The balance between discharging and charging of C2 in T_t is controlled to achieve stable control of the high-voltage bus voltage.

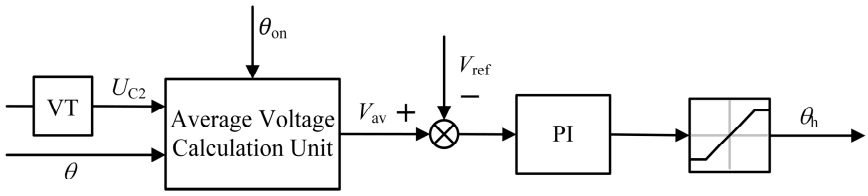

Figure 13. Structure of the boost voltage controller.

4.3. Optimization of Control Parameters

In this article, the coordinated optimization between torque ripple and efficiency is realized by multiobjective optimization control of the SRM, so that the DITC is able to improve the system efficiency while suppressing the torque ripple. For this, the following multiobjective optimization function based on torque ripple and efficiency is constructed:

$$F_{obj}(\theta_{on}, \theta_{off})\big|_{(\omega, T_{ref})} = W_K \frac{K}{K_{min}} + W_E \frac{E_{max}}{E} \tag{2}$$

$$W_K + W_E = 1 \tag{3}$$

where K and E are the torque ripple and drive efficiency in the DITC system, respectively. W_K and W_E are the weighting factors for torque ripple and drive efficiency, respectively. At each torque-speed point (ω, T_{ref}), K_{min} is the minimum torque ripple, and E_{max} is the maximum drive efficiency. K is represented by the following formula:

$$K = \frac{T_{max} - T_{min}}{T_{av}} \times 100\% \tag{4}$$

where T_{max} is the maximum torque, T_{min} is the minimum torque, and T_{av} is the average torque. E is represented by the following formula:

$$E = \frac{P_{out}}{P_{in}} = \frac{\omega T_{av}}{U_{DC} I_{av}} \times 100\% \tag{5}$$

where P_{in}, P_{out}, ω, U_{DC}, and I_{av} are the input power, output power, rotor angular velocity, DC voltage, and average current, respectively.

The multiobjective optimization problem for each operating point is transformed into a problem that satisfies the minimization of the objective function, so as to optimize θ_{on} and θ_{off}, as shown in the following formula:

$$F_{opt}(\theta_{on}^{opt}, \theta_{off}^{opt})\big|_{(\omega, T_{ref})} = \min(W_K \frac{K}{K_{min}} + W_E \frac{E_{max}}{E}) \tag{6}$$

The MATLAB/Simulink model of the novel DITC system is built based on a three-phase 12/8 SRM, and the optimization study of the control parameters is carried out. The basic parameters for the motor are presented in Table 1.

Table 1. Parameters for the experimental motor.

Motor Parameters	Values
Number of stator/rotor poles	12/8
Rated voltage	295 V
Rated power	1.1 kW
Rated speed	2000 r/min
Rated load	5.25 N·m

In order to avoid the complex process of manually seeking optimal control parameters by traversing all angles using a simulation model, a search algorithm was developed for performing angle optimization to calculate the optimal control parameters for each operating point. The execution process of the search algorithm is presented in Figure 14. To guarantee smooth torque transition in the commutation region, the preceding phase should be turned off after the position at which the stator salient pole of the following phase overlaps the center of the rotor groove, i.e., the minimum θ_{off} is set to 15° (θ_{off} (min)). The following phase should be turned on before the preceding phase turns off, so there is a minimum conduction angle of 15° (θ_c (min)). The current of the preceding phase enters the falling inductance region after 22.5° and produces negative torque, so the maximum θ_{off} should be set and maintained at a certain margin. In this analysis, the maximum θ_{off} is set at 21° (θ_{off} (max)). In addition, the minimum and maximum values of θ_{on} are set to −5° (θ_{on} (min)) and 5° (θ_{on} (max)), the minimum and maximum values of T_{ref} are set to 1 N·m (T_{ref} (min)) and 5 N·m (T_{ref} (max)), and the minimum and maximum values of ω are set to 250 r/min (ω (min)) and 1750 r/min (ω (max)). At the end of the search for each operating point, K_{min} and E_{max} are found in the output results, and then the optimal θ_{on} and θ_{off} are gained by calculating the objective function. In this article, torque ripple suppression is the primary objective, and improving the system efficiency is the secondary objective. Thus, W_K is 0.6 and W_E is 0.4. Figure 15 shows the optimized results for θ_{on} and θ_{off} gained by the search algorithm, which is used to establish a lookup table for optimal control of the SRM.

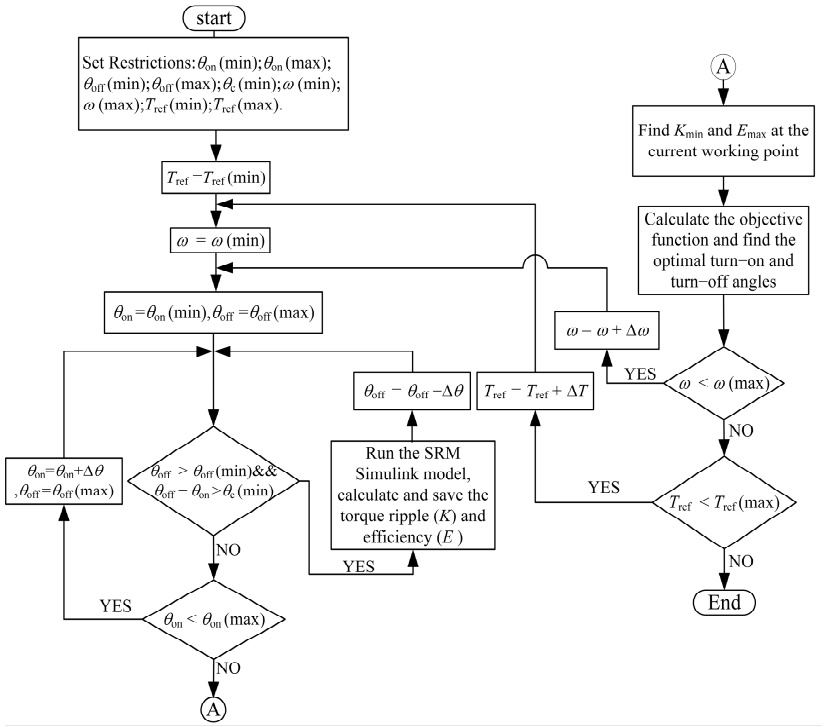

Figure 14. Flow chart of the search algorithm for optimizing control parameters.

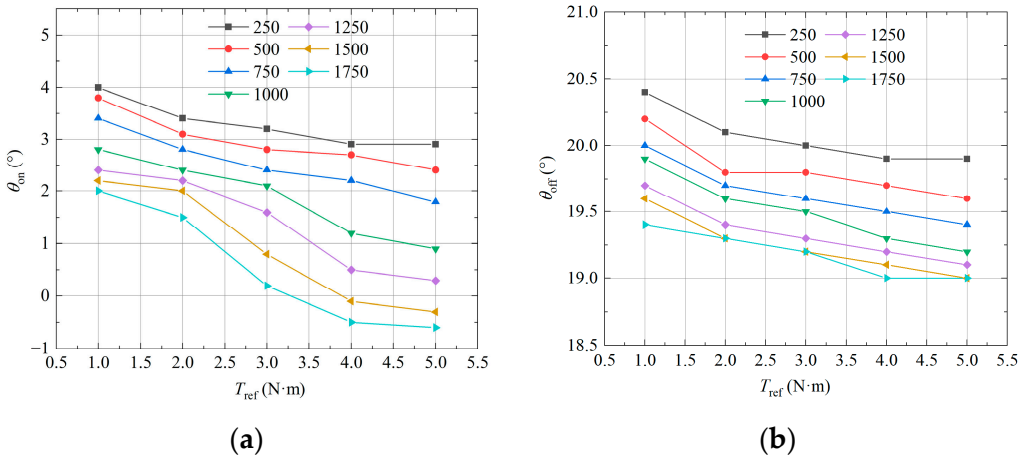

Figure 15. Optimization results for θ_{on} and θ_{off}: (**a**) optimized θ_{on}; (**b**) optimized θ_{off}.

5. Simulation Analysis

For the purpose to study the performance of the novel DITC system, simulation comparison analysis with the conventional DITC system is performed. The conventional DITC system obtains the optimal control parameters using the same multiobjective optimal control method as that used for the novel DITC system.

At a speed of 500 r/min and a load of 5 N·m, Figures 16 and 17 show the simulation waveforms for the two DITC systems with the four hysteresis thresholds set to −0.625, −0.3125, 0.3125, and 0.625 N·m. As can be seen from the simulation results, the torque ripple in the novel DITC system is 22% while that in the conventional DITC system is 27.6%. The simulation waveforms indicate that the conventional DITC for the SRM exhibits significant torque ripple in the commutation region, whereas the novel DITC for the SRM minimizes the torque ripple in this region.

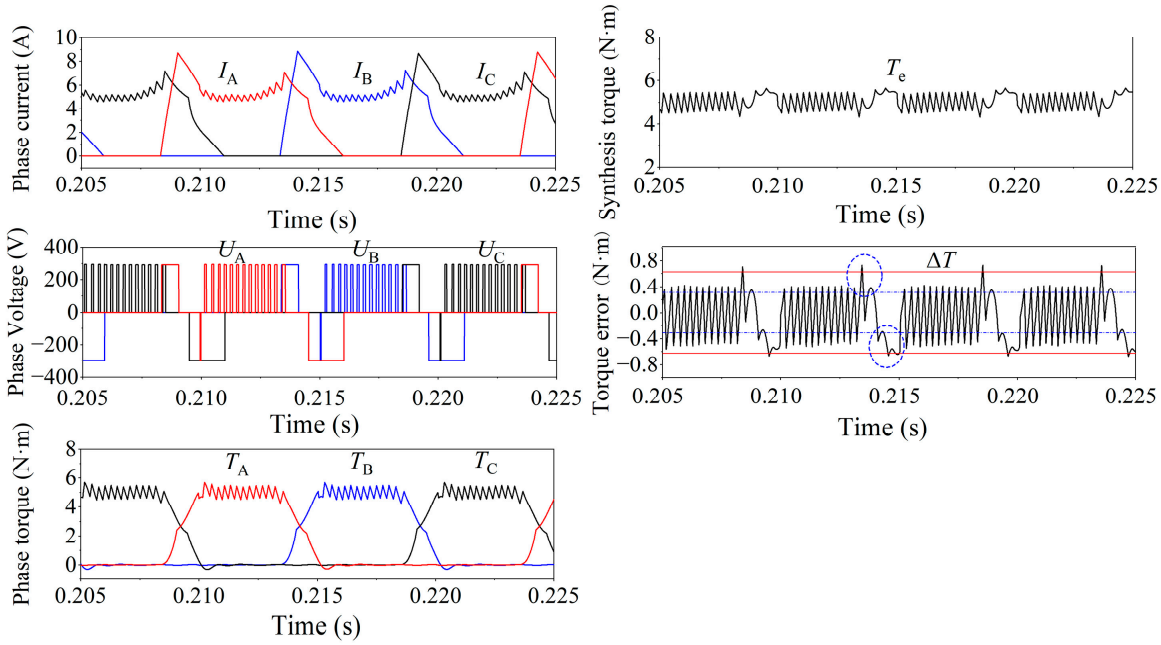

Figure 16. Simulation waveforms in the conventional DITC system at 500 r/min and 5 N·m load.

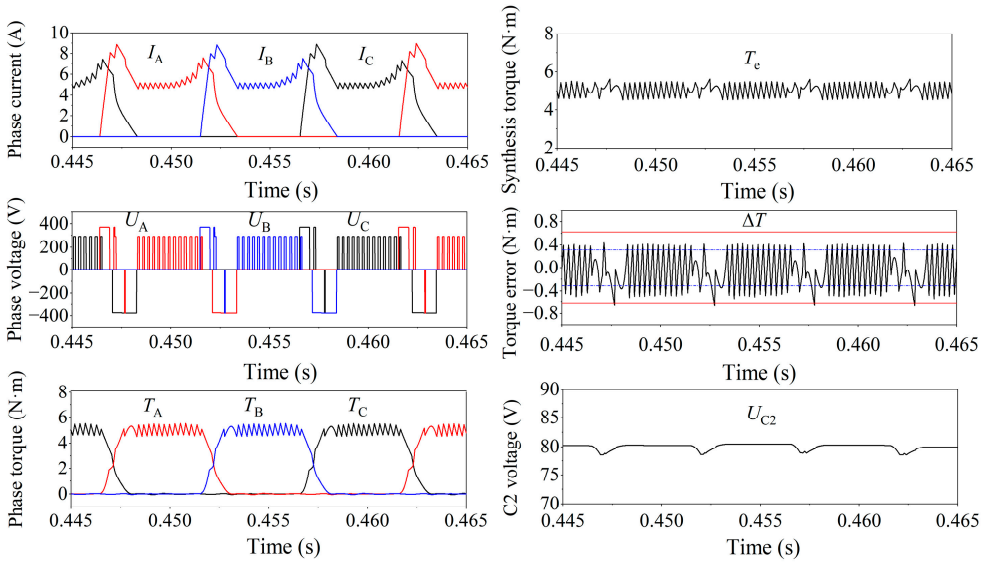

Figure 17. Simulation waveforms in the novel DITC system at 500 r/min and 5 N·m load.

At a speed of 1750 r/min and a load of 2 N·m, Figures 18 and 19 show the simulation waveforms in two DITC systems with the four hysteresis thresholds set to −0.25, −0.125, 0.125, and 0.25 N·m. In accordance with the simulation results, the torque ripple in the novel DITC system is 26.2%, and the torque ripple in the conventional DITC system is 47%, with a 20.8% reduction in torque ripple. Analyzing the simulation waveforms presented in Figure 18 reveals that the DC bus voltage is limited by the AHBC, due to the considerable rotating electromotive force at high speed, which results in the total output torque deviating significantly from the reference torque and the ΔT exceeding the external torque hysteresis thresholds. Moreover, the current in the preceding phase of the commutation region fails to decay to zero promptly, leading to its flow into the negative torque region where it generates significant negative torque. Additionally, the current waveforms of three-phase windings overlap. In contrast, the novel DITC for the SRM maintains great torque-following capability, and the ΔT is effectively controlled within the external torque hysteresis thresholds. Additionally, it enables smaller negative torque levels and current waveforms without three-phase overlap. These improvements are demonstrated in Figure 19.

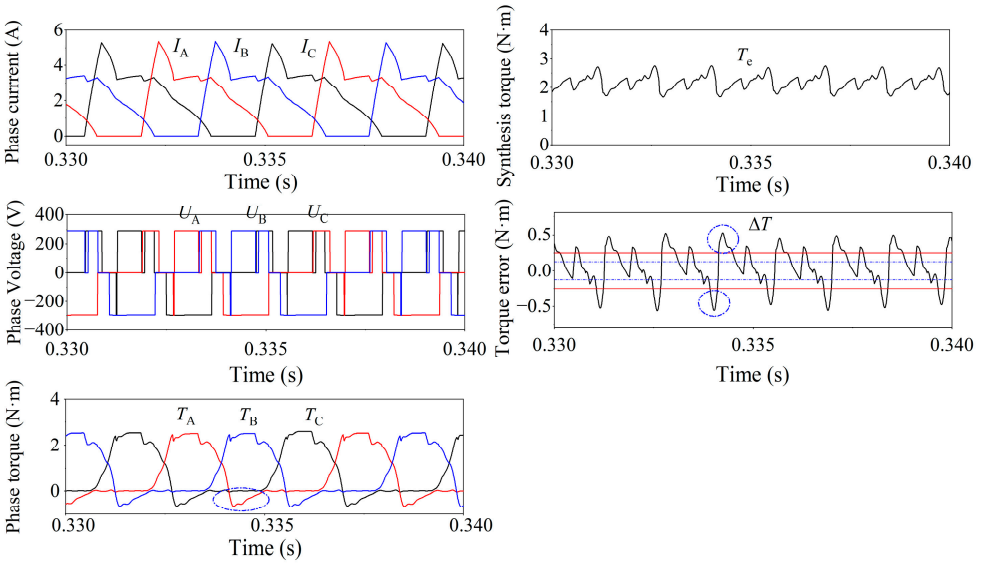

Figure 18. Simulation waveforms in the conventional DITC system at 1750 r/min and 2 N·m load.

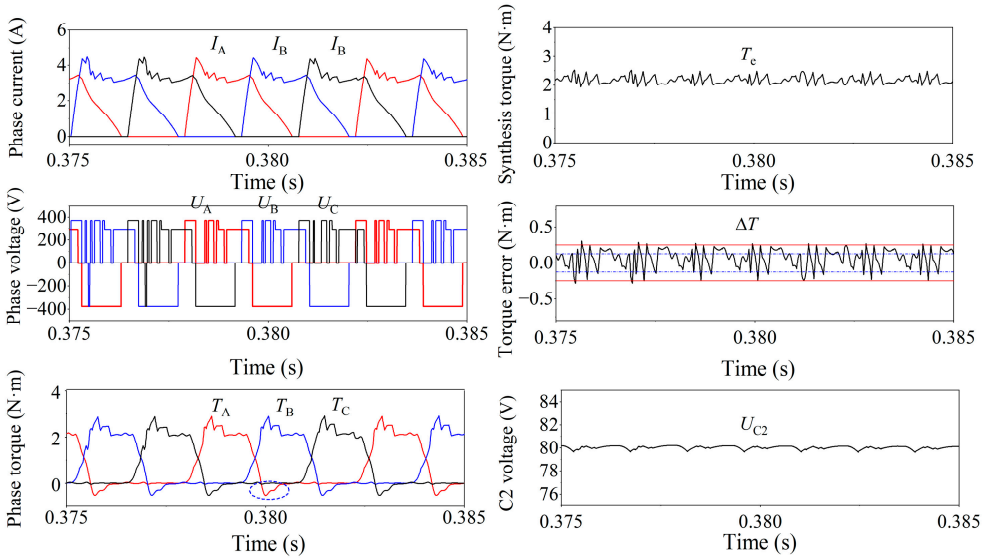

Figure 19. Simulation waveforms in the novel DITC system at 1750 r/min and 2 N·m load.

To further compare the torque ripple for the two DITC systems, the comparative data are given in Tables 2 and 3 for different speeds and different loads. At different speeds, the torque ripple of the novel DITC system is observed to be lower than that of the conventional DITC system. Furthermore, compared to the conventional DITC, the novel DITC for SRM is particularly effective in suppressing torque ripple at high speed, and the torque ripple changes less with increasing speed. These findings indicate that the novel DITC system can maintain smooth torque output in a wide speed range.

Table 2. Torque ripple for the two DITC systems at 2 N·m load.

Speed (r/min)	Load (N·m)	*K* (Conventional DITC) (%)	*K* (Novel DITC) (%)
250	2	23.3	23.2
500	2	24.1	23.2
750	2	27.6	23.4
1000	2	28.1	25.1
1250	2	29.3	25.5
1500	2	31.6	25
1750	2	47	26.2

Table 3. Torque ripple for the two DITC systems at 5 N·m load.

Speed (r/min)	Load (N·m)	*K* (Conventional DITC) (%)	*K* (Novel DITC) (%)
250	5	22.6	20.4
500	5	27.6	22
750	5	30.3	23.2
1000	5	32.7	23.7
1250	5	34.4	25.6
1500	5	42.8	27.8
1750	5	73.7	36.3

6. Experimental Verification

In order to verify the effectiveness of the novel DITC, an experimental platform is constructed, as shown in Figure 20. The experimental motor parameters are consistent with those used in the simulation. The experimental system utilizes the TMS320F28377D core

processor from TI with a sampling period of 10 μs. In addition, the switching frequency of the switching devices is limited to 20 KHz.

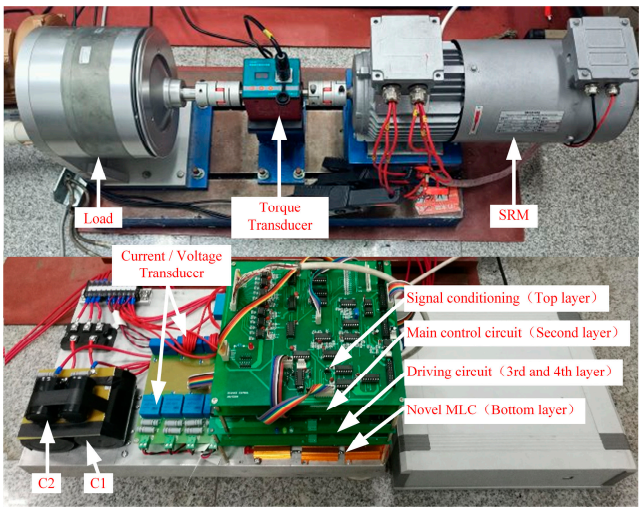

Figure 20. Experiment platform.

Figures 21 and 22 show the experimental waveforms in the two DITC systems at a speed of 1500 r/min and load of 3 N·m, with the four hysteresis thresholds set to −0.6, −0.3, 0.3, and 0.6 N·m, respectively. The torque ripple in the conventional DITC system is calculated to be 64.5%, while it is reduced to 43.3% in the novel DITC system, resulting in a torque ripple reduction of 21.2%.

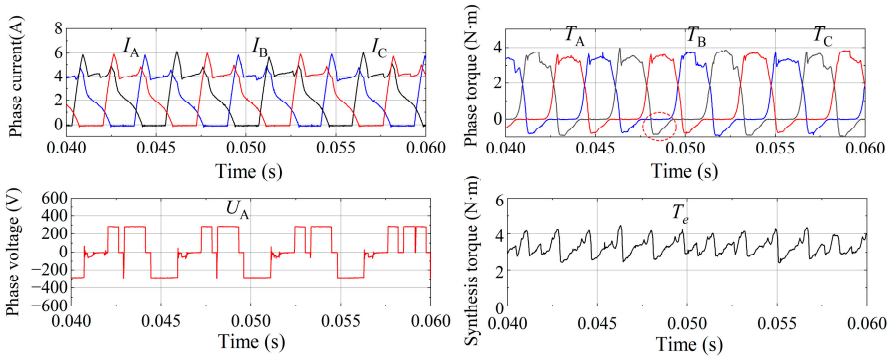

Figure 21. Experimental waveforms in the conventional DITC system at 1500 r/min and 3 N·m load.

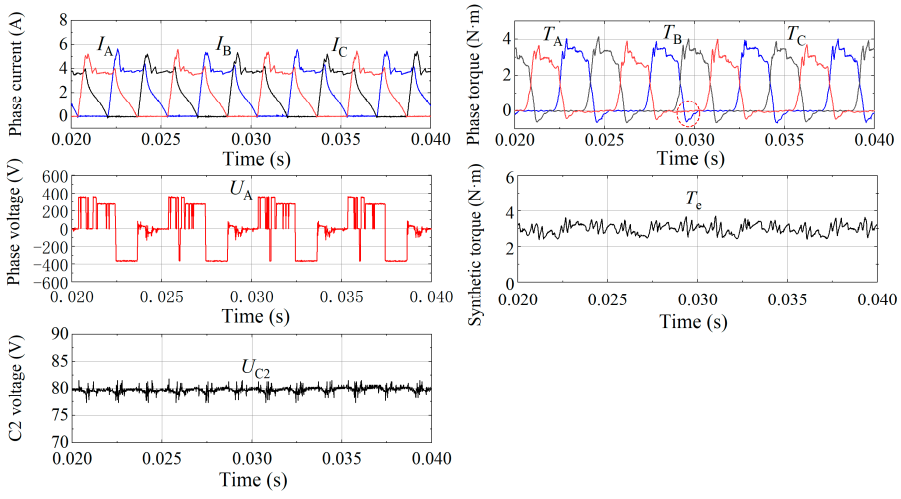

Figure 22. Experimental waveforms in the novel DITC system at 1500 r/min and 3 N·m load.

The experimental waveforms of the conventional DITC system shown in Figure 21 indicate that the phase voltage is almost not chopped, and the motor is close to the single pulse operation mode. This indicates that, at this time, the DC bus voltage is unable to counteract the rotating electric potential of the phase winding, leading to a significant torque ripple and an inability for the output torque to follow the reference value. At the same time, noticeable negative torque is produced, which not only reduces the efficiency of the system but also exacerbates the torque ripple problem. The experimental waveforms of the novel DITC system shown in Figure 22 indicate that the C2 voltage remains stable at 80 V, and the phase voltage undergoes continuous chopping. This demonstrates the system's capability to regulate the output torque to follow the reference value. In addition, the high-voltage demagnetization process effectively suppresses phase current tailing and reduces negative torque.

The measured torque ripple in the experiment is larger than that obtained from the simulation results, mainly due to the fact that the simulation system has ideal conditions, while the experimental system requires higher sampling frequency and switching frequency, and there are some errors in the current sampling and rotor position detection. However, the overall experimental results and waveform laws are generally consistent with the simulation.

Figure 23 gives the experimental efficiency and root-mean-square (RMS) current with different speeds for the two DITC systems at a 3 N·m load. The novel MLC, as it is able to rapidly increase the current in the following phase of the commutation region and rapidly decay the current in the preceding phase of the commutation region, makes efficient use of the rising inductance region to generate positive torque. Therefore, compared to the AHBC, the use of the novel MLC reduces the RMS current through each winding. This results in lower losses in the motor and switching devices and improves the efficiency of the DITC system. Although DITC is beneficial in reducing torque ripple, the efficiency is lower than the ATC. On the one hand, the experiment studies the overall efficiency of the DITC system, and the system losses include the losses of the motor and the converter; on the other hand, the efficiency is usually highest when the motor works at the rated operating point, while the motor speed and carrying loads in the experiment are lower than the rated operating point.

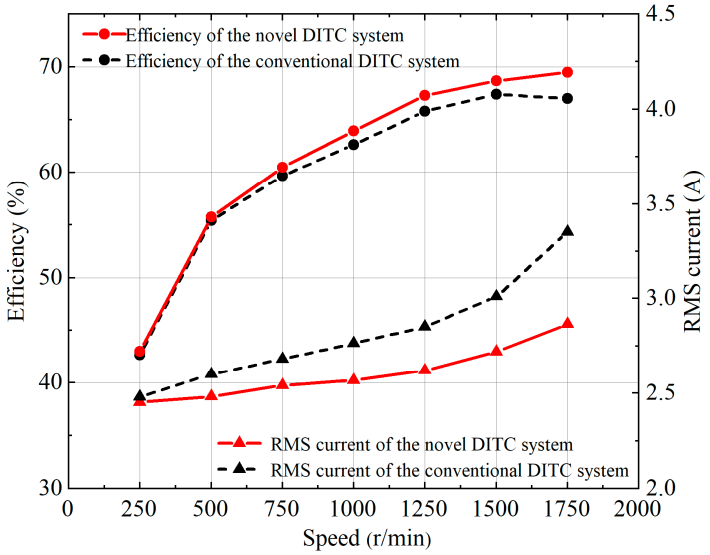

Figure 23. Efficiency and RMS current for the two DITC systems at different speeds.

7. Conclusions

In this paper, a novel MLC is used for direct transient torque control of an SRM, and a novel drive scheme is designed for solving the problem that the torque ripple in the conventional DITC drive system cannot be effectively suppressed.

The high-voltage excitation and high-voltage demagnetization of the novel MLC can overcome the bus voltage limitation of the AHBC, reduce the rising and falling time of the phase winding current, and improve the torque tracking capability of the system. In addition, the novel control strategy based on the torque characteristics at commutation ensures a reasonable distribution of torque between the preceding and following phases. These improvements reduce the torque tracking error, effectively suppress the torque ripple of the SRM, and achieve smooth torque output in a wide speed range. The multiobjective optimization method is also used to find the optimal turn-on and turn-off angle control parameters, which can effectively utilize the rising inductance region to generate positive torque, reduce motor losses, and improve the efficiency of the system.

Although the novel MLC increases the cost of the drive system by adding more switching devices than the AHBC, it is worth it based on the effective improvement in drive performance that the novel drive system brings.

Author Contributions: Formal analysis, Y.C.; funding acquisition, Y.C.; methodology, Y.C. and Z.D.; project administration, Y.C.; coding and testing, Z.D. and Y.L.; writing—original draft, Z.D.; article review and proofreading, Y.C., H.L. and Y.W. All authors have read and agreed to the published version of the manuscript.

Funding: This research was funded by the National Natural Science Foundation of China, grant number 51777137.

Data Availability Statement: All important data are included in the manuscript.

Conflicts of Interest: The authors declare no conflict of interest.

References

1. Aiso, K.; Akatsu, K. Performance Comparison of High-Speed Motors for Electric Vehicle. *World Electr. Veh. J.* **2022**, *13*, 57. [CrossRef]
2. Lan, Y.; Benomar, Y.; Deepak, K.; Aksoz, A.; Baghdadi, M.E.; Bostanci, E.; Hegazy, O. Switched Reluctance Motors and Drive Systems for Electric Vehicle Powertrains: State of the Art Analysis and Future Trends. *Energies* **2021**, *14*, 2079. [CrossRef]
3. Wang, Z.; Ching, T.W.; Huang, S.; Wang, H.; Xu, T. Challenges Faced by Electric Vehicle Motors and Their Solutions. *IEEE Access* **2021**, *9*, 5228–5249. [CrossRef]
4. Vosswinkel, M.; Lohner, A.; Platte, V.; Hirche, T. Design, Production, and Verification of a Switched-Reluctance Wheel Hub Drive Train for Battery Electric Vehicles. *World Electr. Veh. J.* **2019**, *10*, 82. [CrossRef]
5. Faria, C.T.; Santos, F.; Chauvicourt, F.; Orlando, S. Noise Emissions on Switched Reluctance Motors: Evaluation of Different Structural Models. *World Electr. Veh. J.* **2015**, *7*, 179–186. [CrossRef]
6. Kusumi, T.; Hara, T.; Umetani, K.; Hiraki, E. Phase-current Waveform for Switched Reluctance Motors to Eliminate Input-current Ripple and Torque Ripple in Low-power Propulsion below Magnetic Saturation. *IET Power Electron.* **2020**, *13*, 3351–3359. [CrossRef]
7. Dorneles Callegaro, A.; Liang, J.; Jiang, J.W.; Bilgin, B.; Emadi, A. Radial Force Density Analysis of Switched Reluctance Machines: The Source of Acoustic Noise. *IEEE Trans. Transp. Electrific.* **2019**, *5*, 93–106. [CrossRef]
8. Qiao, W.; Han, S.; Diao, K.; Sun, X. Optimization Design and Control of Six-Phase Switched Reluctance Motor with Decoupling Winding Connections. *Appl. Sci.* **2022**, *12*, 8801. [CrossRef]
9. Choi, Y.K.; Yoon, H.S.; Koh, C.S. Pole-Shape Optimization of a Switched-Reluctance Motor for Torque Ripple Reduction. *IEEE Trans. Magn.* **2007**, *43*, 1797–1800. [CrossRef]
10. Abunike, C.E.; Okoro, O.I.; Aphale, S.S. Intelligent Optimization of Switched Reluctance Motor Using Genetic Aggregation Response Surface and Multi-Objective Genetic Algorithm for Improved Performance. *Energies* **2022**, *15*, 6086. [CrossRef]
11. De Paula, M.V.; Williamson, S.S.; Barros, T.A. Four-Quadrant Model Following Sliding Mode Cruise Control for SRM With DITC Applied to Transportation Electrification. *IEEE Trans. Transp. Electrif.* **2022**, *8*, 3090–3099. [CrossRef]
12. De Paula, M.V.; Barros, T.A.; Moreira, H.S.; Catata, E.O.H.; Villalva, M.G.; Filho, E.R. A Dahlin Cruise Control Design Method for Switched Reluctance Motors With Minimum Torque Ripple Point Tracking Applied in Electric Vehicles. *IEEE Trans. Transp. Electrif.* **2021**, *7*, 730–740. [CrossRef]
13. Song, S.; Huang, S.; Zhao, Y.; Zhao, X.; Duan, X.; Ma, R.; Liu, W. Torque Ripple Reduction of Switched Reluctance Machine With Torque Distribution and Online Correction. *IEEE Trans. Ind. Electron.* **2023**, *70*, 8842–8852. [CrossRef]
14. Hannoun, H.; Hilairet, M.; Marchand, C. Design of an SRM Speed Control Strategy for a Wide Range of Operating Speeds. *IEEE Trans. Ind. Electron.* **2010**, *57*, 2911–2921. [CrossRef]

15. Hamouda, M.; Abdel Menaem, A.; Rezk, H.; Ibrahim, M.N.; Számel, L. Comparative Evaluation for an Improved Direct Instantaneous Torque Control Strategy of Switched Reluctance Motor Drives for Electric Vehicles. *Mathematics* **2021**, *9*, 302. [CrossRef]
16. Fang, G.; Pinarello Scalcon, F.; Xiao, D.; Vieira, R.; Grundling, H.; Emadi, A. Advanced Control of Switched Reluctance Motors (SRMs): A Review on Current Regulation, Torque Control and Vibration Suppression. *IEEE Open J. Ind. Electron. Soc.* **2021**, *2*, 280–301. [CrossRef]
17. Gribble, J.J.; Kjaer, P.C.; Miller, T.J.E. Optimal Commutation in Average Torque Control of Switched Reluctance Motors. *IEE Proc. -Electr. Power Appl.* **1999**, *146*, 2–10. [CrossRef]
18. Usman Jamil, M.; Kongprawechnon, W.; Chayopitak, N. Average Torque Control of a Switched Reluctance Motor Drive for Light Electric Vehicle Applications. *IFAC-PapersOnLine* **2017**, *50*, 11535–11540. [CrossRef]
19. Hamouda, M.; Szamel, L.; Alquraan, L. Maximum Torque per Ampere Based Indirect Instantaneous Torque Control for Switched Reluctance Motor. In Proceedings of the 2019 International IEEE Conference and Workshop in Óbuda on Electrical and Power Engineering (CANDO-EPE), Budapest, Hungary, 20–21 November 2019; pp. 47–54.
20. Cai, H.; Wang, H.; Li, M.; Shen, S.; Feng, Y.; Zheng, J. Torque Ripple Reduction for Switched Reluctance Motor with Optimized PWM Control Strategy. *Energies* **2018**, *11*, 3215. [CrossRef]
21. Ye, J.; Bilgin, B.; Emadi, A. An Offline Torque Sharing Function for Torque Ripple Reduction in Switched Reluctance Motor Drives. *IEEE Trans. Energy Convers.* **2015**, *30*, 726–735. [CrossRef]
22. Qi, H.; Zhang, T.; Li, Z.; Wei, Y. SRM Torque Ripple Minimization Based on Direct Instantaneous Torque Control. *Trans. China Electrotech. Soc.* **2007**, *7*, 136–140.
23. Inderka, R.B.; De Doncker, R.W.A.A. DITC-Direct Instantaneous Torque Control of Switched Reluctance Drives. *IEEE Trans. Ind. Appl.* **2003**, *39*, 1046–1051. [CrossRef]
24. De Paula, M.V.; Barros, T.A. A Sliding Mode DITC Cruise Control for SRM With Steepest Descent Minimum Torque Ripple Point Tracking. *IEEE Trans. Ind. Electron.* **2022**, *69*, 151–159. [CrossRef]
25. Xue, X.D.; Cheng, K.W.E.; Ho, S.L. Optimization and Evaluation of Torque-Sharing Functions for Torque Ripple Minimization in Switched Reluctance Motor Drives. *IEEE Trans. Power Electron.* **2009**, *24*, 2076–2090. [CrossRef]
26. Liu, L.; Zhao, M.; Yuan, X.; Ruan, Y. Direct Instantaneous Torque Control System for Switched Reluctance Motor in Electric Vehicles. *J. Eng.* **2019**, *16*, 1847–1852. [CrossRef]
27. Von Hoegen, A.; Woerndle, A.; De Doncker, R.W. Implementation of PWM-Based Direct Instantaneous Torque Control with Duty Cycle Interlock for a Switched Reluctance Machine. In Proceedings of the International Conference on Electrical Machines and Systems (ICEMS), Hamamatsu, Japan, 24–27 November 2020; pp. 754–759.
28. Zhu, Y.; Zhang, G.; Huang, Y. PWM-Based Direct Instantaneous Torque Control of Switched Reluctance Machine. *Trans. China Electrotech. Soc.* **2017**, *32*, 31–39.
29. Cheng, Y.; Cao, X.-X.; Zhang, Y.-L. Hysteresis-PWM Direct Instantaneous Torque Control of Switched Reluctance Motor. *Electr. Mach. Control* **2020**, *24*, 74–82.
30. Sun, Q.; Wu, J.; Gan, C. Optimized Direct Instantaneous Torque Control for SRM with Efficiency Improvement. *IEEE Trans. Ind. Electron.* **2021**, *68*, 2072–2082. [CrossRef]
31. Li, Z.; Wei, Y.; Kan, Z.; Qi, H. Direct Instantaneous Torque Control of SRM Using Four-Level Converter. *Trans. China Electrotech. Soc.* **2007**, *22*, 144–149.
32. Sun, Q.; Wu, J.; Gan, C.; Shen, M.; Wang, J.; Sun, H. Multi-Level Converter-Based Torque Sharing Function Control Strategy for Switched Reluctance Motors. In Proceedings of the 19th International Conference on Electrical Machines and Systems (ICEMS), Chiba, Japan, 13–16 November 2016; pp. 1–5.